



# The multitemporal landslide inventory map of the Collazzone study area, central Italy

5 Francesca Ardizzone<sup>1</sup>, Mauro Cardinali<sup>1</sup>, Federica Fiorucci<sup>1</sup>

<sup>1</sup>CNR – IRPI, Via della Madonna Alta 126, 06128, Perugia, Italy

*Correspondence to:* Francesca Ardizzone ([francesca.ardizzone@cnr.it](mailto:francesca.ardizzone@cnr.it))

**Abstract.** Multitemporal landslide inventory maps are an essential source of information for many research and applications. This type of landslide map provides information for analyzing the spatial and temporal distribution of the landslides, their potential interaction with the built environment, their contribution to landscape dynamics, and their response to the triggers over time. The acquisition of the temporal information of landslide evolution provides a fundamental step for hazard evaluation. Despite the essential value of multitemporal landslide inventory maps, their dissemination is rare. This is due to the time-consuming nature of their preparation. In this paper we present the multitemporal landslide inventory map for a 79 km<sup>2</sup> area in the Umbria region (central Italy). The inventory contains more than 3,500 landslides classified according to relative age, type of movement, and estimated depth. The landslide mapping was carried out by interpreting stereoscopic aerial photographs taken in 1941, 1954, 1977, 1985, and 1997, as well as stereo satellite images taken in 2010, 2013, and 2014. The inventory was further updated through several field checks conducted in 1999, 2004, 2005, and 2020, and by interpreting the images available on Google Earth (2011, 2012, 2015, 2015, 2015, 2019, 2021, 2022 and 2023). Landslides were mapped according to rigorous and reproducible criteria applied by a team of expert geomorphologists. The dataset consists of a digital archive including twenty-nine layers, that is available at <https://doi.org/10.5281/zenodo.18980281>.

## 1 Introduction

A landslide inventory map (LIM) records the location and, where known, the date of occurrence and the types of mass movements that have left discernible traces in an area (Guzzetti et al., 2000; Pašek, 1975). Landslide inventory maps are crucial for the following purposes (Guzzetti et al., 2012): (i) recording the extent of landslide phenomena in a certain area; (ii) evaluating landslide susceptibility, hazard, and risk; (iii) investigating the distribution, type and patterns of landslides; and (iv) studying the evolution of landscapes. Among the different types of LIMs (Ardizzone et al., 2023; Guzzetti et al., 2012) the multitemporal landslide inventory map (M-LIM) shows the location and types of landslides triggered by multiple events over longer periods (e.g., years to decades) and portrays their recent evolution in space and time (Galli et al., 2008). A



30 multitemporal inventory map allows to investigate the spatial and temporal evolution of landslides in several different time periods showing areas with different frequency of landslide occurrence (Zumpano et al., 2021). Moreover, the temporal dimension of a multitemporal landslide inventory map is essential for the evaluation of the landslide hazard.

Galli et al., 2008 showed that a multi-temporal inventory prepared through the systematic and simultaneous interpretation of several sets of stereo aerial photographs of different vintages, supplemented by extensive geological and geomorphological field surveys, is superior to (i.e., more reliable than) geomorphological or reconnaissance inventories prepared for the same study area. However, due to the time required to complete a multi-temporal inventory, such a type of map cannot be effectively prepared for a large region, extending for thousands of square kilometers. Consequently, multitemporal landslide inventory maps have been prepared for areas of limited size (Cardinali et al., 2002; Zumpano et al., 2021). Examples of multitemporal landslide inventory maps prepared for large area were presented in 2005 (Guzzetti et al., 2005) for a 275 km<sup>2</sup> study area located in in the southern Lombardy region (northern Italy), in 2006 (Guzzetti et al., 2006b) for a 79 km<sup>2</sup> study area in central Italy and in 2007 (Cardinali et al., 2007) for a 590 km<sup>2</sup> study area in the central Abruzzo region (central Italy). These multi-temporal landslide maps were prepared by interpreting different sets of stereo aerial photographs (from 2 to 5 sets) taken in the period from 1941 through 1997, and field surveys.

Traditionally, multi-temporal landslide inventories have been compiled through the interpretation of multiple sets of aerial photographs. However, recent studies have increasingly integrated additional data sources. Del Ventisette et al., 2014 presented the results obtained, in two study areas in northern Italy, by the interpretation of A-DInSAR satellite dataset, spanning from 1995 through 2009 and their integration with geological and geomorphological data to obtain a multi-temporal updating of landslide inventory map. Recently, Fernández et al., 2021 used aerial photogrammetry and LiDAR techniques to analyze landslide activity over a long-time span (over 32 years), from 1984 to 2001 in a 51 km<sup>2</sup> study area in Spain. Amatya et al., 2024 used high-resolution satellite imagery to generate a multitemporal landslide inventory for the Arun River Basin, Nepal. The inventory represents a yearly record of landslides from 2011 through 2020. (Li et al., 2024), proposed an innovative unsupervised learning method (called PluTsa) for multiple temporal landslide inventory mapping in Japan by using Planet Scope imagery acquired in May 2019, in October 2020, in August 2021 and in October 2022.

Information on landslide locations, types, and sizes, combined with data on temporal occurrence, is crucial to evaluate the hazard posed by landslides. Nevertheless, multitemporal landslide maps are rare and their recent increase is due to the availability of remote sensing technology and the use of artificial intelligence models (Bhuyan et al., 2023b). (Bhuyan et al., 2023a), used Deep Transfer Learning approach applied to High Resolution Planet Lab images, spanning from 2009 through 2021, to generate annual landslide inventories in view of the preparation of a multitemporal landslide inventory map.

In this paper we present the multitemporal landslide inventory map prepared for the Collazzone study area, in Umbria region, central Italy, an area historically affected by shallow and deep landslides. The landslide inventory map was produced using multiple data sources. The inventory was prepared through the interpretation of five sets of stereoscopic aerial photographs, taken in 1941, 1954, 1977, 1985, 1997, of stereo satellite images taken in 2010, 2013 and 2014. The inventory was updated through several field checks conducted in 1999-2000, 2004, 2005, 2020 and through the interpretation of the



images available on Google Earth: 2011-04-02, 2012-05-10, 2015-03-14, 2015-07-08, 2018-04-08, 2019-10-08, 2021-04-28, 2022-03-23, 2023-05-30. The multitemporal landslide inventory map of Collazzone (M-LIM-C) represents the product of a work that began in the early 2000s. The M-LIM-C was used to perform several studies such as evaluation of hazard and risk (Guzzetti et al., 2006b, a, 2009a; Lombardo et al., 2020a; Mergili et al., 2014; Rossi et al., 2010); sediment mobilization rate (Fiorucci et al., 2011; Guzzetti et al., 2009b); understanding the “legacy effects” of the landslides (Samia et al., 2017a, b, 2018, 2020).

## 2 Study area

The Collazzone area, located in central Umbria (Italy), extends for about 79 km<sup>2</sup> with elevations ranging from 145 m along the Tiber River floodplain to 634 m at Monte di Grutti (Figure 1A). The landscape is predominantly hilly, and the lithology and the attitude of bedding planes control the morphology of the slopes. North-south valleys are shorter, asymmetrical, and parallel to the main direction of the bedding planes, whereas east-west valleys are longer, symmetrical, and mostly perpendicular to the direction of the bedding planes. Sedimentary rocks crop out in the area including (Figure 1B): (i) alluvial deposits, chiefly along the main valley bottoms, (ii) continental gravel, sand and clay, Plio-Pleistocene in age, (iii) travertine deposits, Pleistocene in age, (iv) layered sandstone and marl in various percentages, Miocene in age, and (v) thinly layered limestone, Lias to Oligocene in age (Conti et al., 1977; Servizio Geologico Nazionale, 1980; Cencetti, 1990; Barchi et al., 1991). The terrain is hilly, valleys are asymmetrical, and slopes are controlled by lithology and the attitude of bedding. Soil in the area ranges in thickness from a few decimeters to more than one meter, they have a fine or medium texture, and exhibit a xeric moisture regime, typical of the Mediterranean climate with precipitation falling mostly in the period from October to December and from February to May. Annual average rainfall is about 740 mm (from 2000 to 2024) measured at the Collepepe rain gauge (Fig. 1A). The land use includes cropland, forest, vineyard and orchard, and urban areas (Fig. 1C). Landslides are abundant and are caused primarily by meteorological triggers, including prolonged rainfall and rapid snowmelt (January 1997). They can be classified as rapid to very slow, shallow soil slides and flows, deep-seated slides and flows, and compound movements (Galli et al., 2008; Guzzetti et al., 2006a, b).

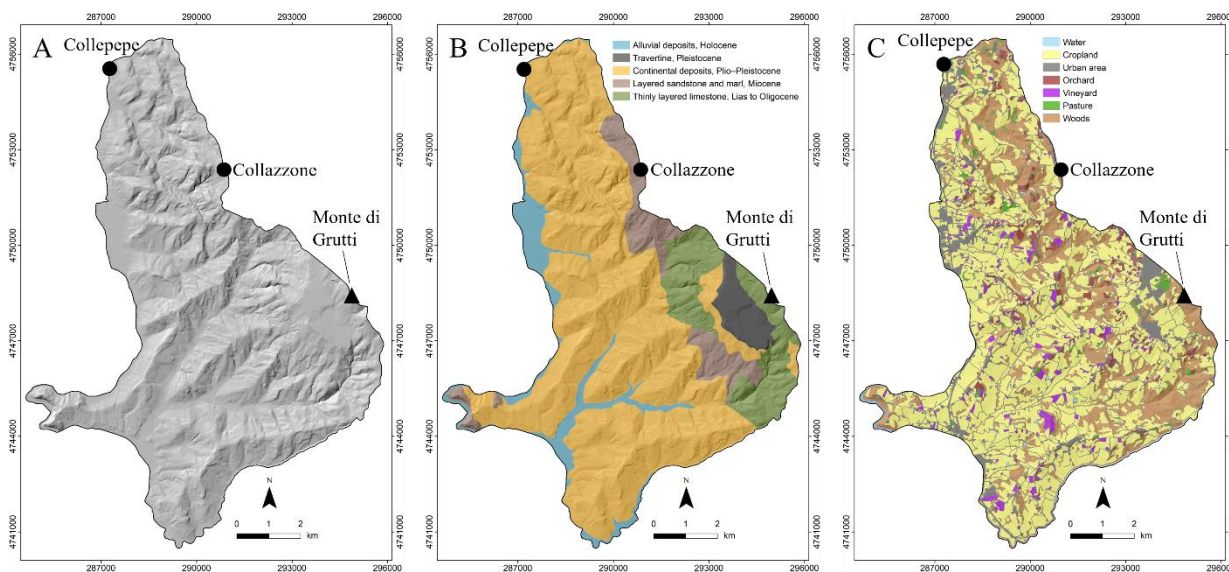


Figure 1: Collazzone study area: A) shaded relief; B) lithological map; c) land use map.

### 3 Material and method

The preparation of M-LIM-C has been ongoing for nearly two decades, employing various methods for landslide mapping. The inventory is periodically updated following significant landslide events and is subject to regular field checks to validate and refine the mapped information. We employed a multi-stage approach rather than a single procedure, with activities conducted overtime (Fig. 2). The overall work consisted of three main stages: (i) data acquisition (e.g., landslide interpretation and field survey), (ii) data editing (e.g. digitalization in GIS environment), and (iii) finalizing the results (i.e., the geodatabase).

The M-LIM-C was prepared at a 1:10,000 scale through the interpretation of five sets of aerial photographs (Table 1) and extensive geological and geomorphological field mapping (layers A<sub>0</sub> to E<sub>2</sub> in Table 1). This initial work constituted the core of the landslide inventory map, which has been subsequently expanded and updated over time. The map was updated in the period from September 2003 through April 2004 through field surveys conducted following periods of prolonged rainfall to map landslides triggered by heavy rainfall (layers F<sub>1</sub> to F<sub>4</sub> in Table 1). Between 2009 and 2014, the inventory was improved by incorporating landslide maps prepared using VHR stereo satellite imagery (layers G<sub>1</sub>, G<sub>2</sub>, G<sub>5</sub> and G<sub>6</sub> in Table 1). In December 2020, a field survey mapped new landslides triggered by several days of intense rainfall. Additional landslides were identified through Google Earth at different dates (Table 1).

Figure 2 synthesizes the phases of the activities carried out to obtain the M-LIM-C. The first phase consisted in the acquisition of data, namely the identification of landslides. The investigation and identification of the landslides have been conducted using two methods: i) image interpretation of aerial stereo-photographs (Galli et al., 2008), stereo satellite images (Ardizzone et al., 2013) and satellite images available on Google Earth Pro application; and ii) field surveys conducted



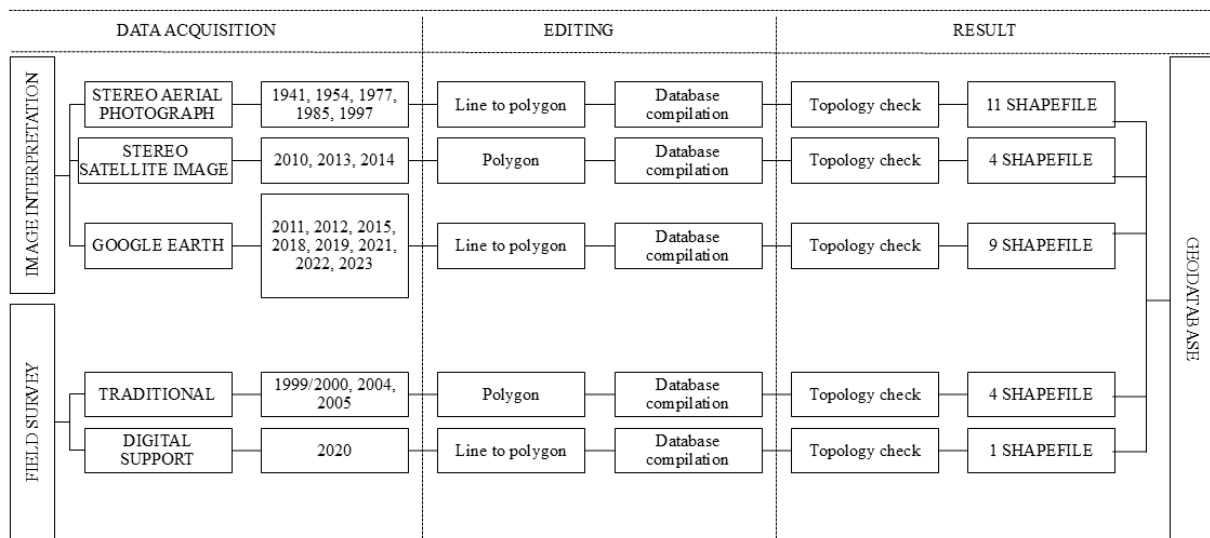
driving along the main and secondary roads and mapping landslides in the field at 1:10 000 scale using topographic base maps (Cardinali et al., 2006). In the last ten years the mapping of the landslides taking notes directly on site on Google Earth, as described by Santangelo et al., 2023.

110 The editing phase resulted in geometrically and topologically correct shapefiles (EPSG: 23033), whose preparation methods have evolved over time in parallel with advancements in GIS software. Initially, in the early 2000s when aerial photography and digital stereoscopic viewing systems were not yet available, landslides were drawn by hand on transparent plastic sheets overlaid on paper stereoscopic aerial photographs and then transferred to 1:10,000 scale topographic base maps on additional transparent sheets, which were subsequently scanned for digital use (layers A<sub>0</sub> to E<sub>2</sub> in Table 1). With the advent of digital

115 satellite imagery, landslides began to be delineated directly on the computer screen (layers G<sub>1</sub>, G<sub>2</sub>, G<sub>5</sub> and G<sub>6</sub> in Table 1) (Ardizzone et al., 2013, 2023; Galli et al., 2008). In the case of field surveys, shapefile production involved mapping landslides on-screen using digital raster topographic maps (1:10,000 scale), with field photographs aiding in the spatial positioning and in the characterization of the type and size of mass movements (Ardizzone et al., 2007; Cardinali et al., 2006). In recent years Google Earth was used to map directly landslides in the field to be converted into polygons in GIS

120 once back in the laboratory (layers G<sub>7</sub>-G<sub>10</sub>, G<sub>12</sub> and G<sub>6</sub>-G<sub>14</sub> in Table 1).

The final phase consisted in the implementation of the attribute table, based on a defined legend, after the control of the topology correctness. The final inventory includes 27 polygon shapefiles spanning from 1941 to 2023 and two polygon shapefiles related to landslides that are very old and old corresponding to a geomorphological inventory (A<sub>0</sub> and A<sub>1</sub> in Table 1).



125

**Figure 2: Schema of the work carried out to obtain the M-LIM-C. The activity includes three phases: data acquisition, editing and results. The two methods used to map the landslides are: photo interpretation and field surveys.**



The stereo paper aerial photographs used to compile the multi-temporal map span from 1941 through 1997, and range in scale from 1:13,000 to 1:33,000. A team of two geomorphologists carried out the interpretation of the aerial photographs. Each stereo pair was analyzed using a mirror stereoscope (4× magnification) and a continuous-zoom discussion stereoscope (3× to 20× magnification). Both instruments allowed simultaneous viewing and mapping of the same stereo pair by both interpreters. The interpreters used all morphological, geological and landslide information available from published maps, previous work carried out in the same area, and discussion with other geomorphologists. Care was taken to identify areas where morphology had changed in response to mass movements, and to minimize interpretation errors caused by land use changes or by differences in the viewing geometry of aerial photographs taken at different dates. Extensive field checks were conducted to check the landslides mapped.

In the GIS database, landslides attributed to a single date (e.g., a rainfall event) or period were stored separately. Following this procedure, new and active landslides recognized, e.g. in the 1977 aerial photographs were stored in a separate layer than the landslides mapped as inactive in the same photographs. In each of the five sets of aerial photographs used to prepare the multi-temporal inventory, we separated the landslides that appeared “fresh” (i.e., showing recent signs of activity) in the aerial photographs, from pre-existing or dormant landslides. The “fresh” slope failures were assigned the date (i.e., the year) corresponding to the aerial photographs in which they were identified (i.e. 1941, 1954, 1977, 1985, 1997). The remaining slope failures (i.e., “non-fresh” landslides) were assigned to the time interval between two consecutive aerial surveys. Although these landslides no longer appeared fresh in the more recent imagery, they exhibited morphological changes relative to one or more of the earlier photo sets, indicating that they occurred during the inter-survey period (i.e. 1941-1954, 1954-1977, 1977-1985, 1985-1997). As a result, for a single set of aerial photographs, multiple layers were obtained “fresh or active” layer and “inter-period layer” (for example, the landslides identified fresh in the 1977 and 1954 aerial photographs are landslides that were probably triggered by an intense or prolonged weather event in the year of the photograph. These landslides are considered active landslides. The 1954-1977 inter-period landslides are landslides that were not present in the 1954 photographs and present but without apparent freshness in the 1977 photographs. These landslides likely were triggered by one or more intense or prolonged weather events during the period between 1954 and 1977). The procedure required intensive and time-consuming GIS work to identify and correct topological and geographical errors, such as overlapping polygons, gaps between adjacent features, misalignments with base maps, and inconsistencies in attribute data. This step was essential to ensure the spatial accuracy and consistency of the landslide inventory over multiple temporal layers. The obtained GIS database stores information on landslides attributed to 11 different dates or periods including two layers referred to old and very old landslides, namely  $A_0$  and  $A_1$  which could be considered (Guzzetti et al., 2006c).

The inventory map obtained from the analysis of the aerial photographs was updated to include the period from 1998 onward through field surveys conducted after periods of prolonged rainfall. Starting in 2005, the use of satellite imagery—including very high resolution (VHR) stereo satellite images and the Google Earth platform—enabled near-annual updates of the inventory. The investigation of the VHR stereoscopic satellite images was conducted using the StereoMirror™ technology



for block orientation, and Stereo Analyst for ArcGIS® SW for image visualization and landslide mapping (Ardizzone et al., 2013). The 3-D views of the topographic surface created with the oriented satellite images, were investigated to identify the landslides related to the rainfall that occurred in 2010, 2013 and 2014 years (G<sub>1</sub>, G<sub>2</sub>, G<sub>5</sub> and G<sub>6</sub> layers in Table 1). The digitalization of the landslides occurred simultaneously with the study of the stereo pair in a polygon shapefile. In the last ten years Google Earth Pro has provided imagery at nearly annual intervals. For years lacking aerial or satellite coverage, Google Earth was examined, and the available imagery was visually inspected. Landslides were digitized directly in KML format as polygons and subsequently converted into polygon shapefiles using GIS software (see Table 1 for the corresponding layers).

**Table 1.** List of the layers included in the M-LIM-C. ELA: estimated landslide age. P-I: photo interpretation. F-S: field survey. GSD: ground sample distance. The letters from A to E indicate the layer prepared by the photointerpretation of the stereo-aerial photographs. The letter F indicates the layers prepared through field surveys. The letter G indicates the layers prepared using satellite imagery.

LAYER	ELA	METHOD	SOURCE	MODE	DATE	TYPE	SCALE
A <sub>0</sub>	very old	P-I	Aerial photos	Stereo	Summer 1941	Panchromatic	1:18,000
A <sub>1</sub>	older than 1941	P-I	Aerial photos	Stereo	Summer 1941	Panchromatic	1:18,000
A <sub>2</sub>	1941	P-I	Aerial photos	Stereo	Summer 1941	Panchromatic	1:18,000
B <sub>1</sub>	1941–1954	P-I	Aerial photos	Stereo	Spring/Summer 1954	Panchromatic	1:33,000
B <sub>2</sub>	1954	P-I	Aerial photos	Stereo	Spring/Summer 1954	Panchromatic	1:33,000
C <sub>1</sub>	1954-1977	P-I	Aerial photos	Stereo	Summer 1977	Color	1:13,000
C <sub>2</sub>	1977	P-I	Aerial photos	Stereo	Summer 1977	Color	1:13,000
D <sub>1</sub>	1977-1985	P-I	Aerial photos	Stereo	July 1985	Panchromatic	1:15,000
D <sub>2</sub>	1985	P-I	Aerial photos	Stereo	July 1985	Panchromatic	1:15,000
E <sub>1</sub>	1985-1997	P-I	Aerial photos	Stereo	April 1997	Panchromatic	1:20,000
E <sub>2</sub>	1797	P-I	Aerial photos	Stereo	April 1997	Panchromatic	1:20,000
F <sub>1</sub>	1999-2000	F-S	NA	NA	NA	NA	1:10,000
F <sub>2</sub>	May 2004	F-S	NA	NA	May 2004	NA	1:10,000
F <sub>3</sub>	December 2004	F-S	NA	NA	December 2004	NA	1:10,000

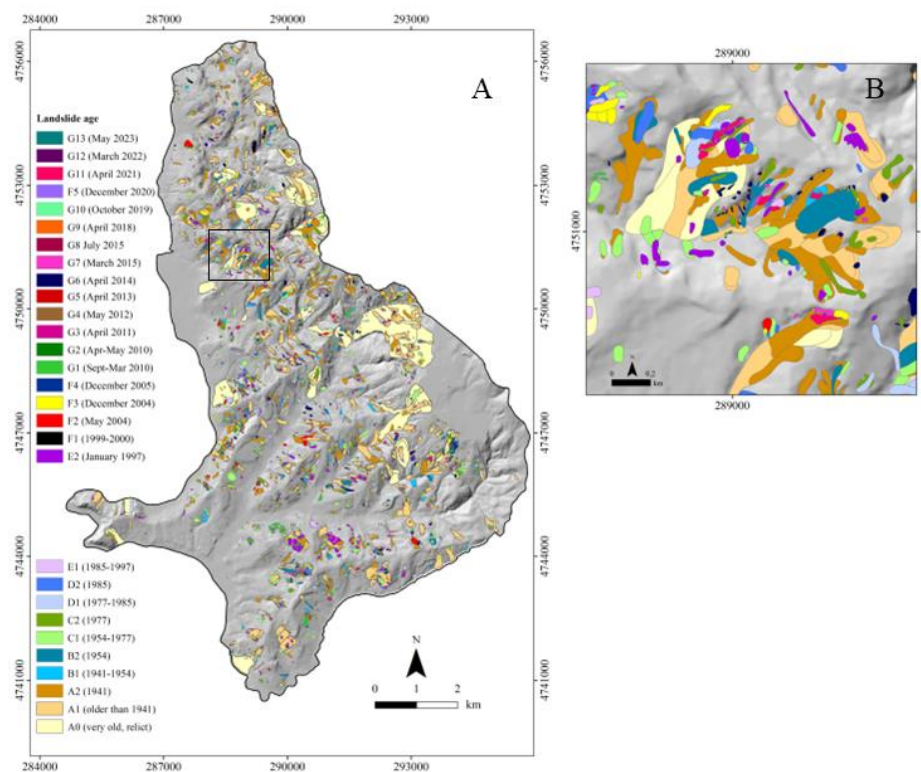


F <sub>4</sub>	December 2005	F-S	NA	NA	December 2005	NA	1:10,000
G <sub>1</sub>	Sept-Mar 2010	P-I	GeoEye-1	Stereo	2009-08-12	Panchromatic	GSD = 0.41 m
			WorldView-1	Stereo	2010-03-08	Panchromatic	GSD = 0.50 m
G <sub>2</sub>	Apr-May 2010	P-I	GeoEye-1	Stereo	2010-05-27	Panchromatic	GSD = 0.41 m
G <sub>3</sub>	April 2011	P-I	Google Earth	NA	2011-04-02	NA	NA
G <sub>4</sub>	May 2012	P-I	Google Earth	NA	2012-05-10	NA	NA
G <sub>5</sub>	April 2013	P-I	GeoEye-1	Stereo	2013-04-13	Panchromatic	GSD = 0.50 m
G <sub>6</sub>	April 2014	P-I	WorldView-2	Stereo	2014-04-14	Panchromatic	GSD = 2.00 m
G <sub>7</sub>	March 2015	P-I	Google Earth	NA	2015-03-14	NA	NA
G <sub>8</sub>	July 2015	P-I	Google Earth	NA	2015-07-08	NA	NA
G <sub>9</sub>	April 2018	P-I	Google Earth	NA	2018-04-08	NA	NA
G <sub>10</sub>	October 2019	P-I	Google Earth	NA	2019-10-08	NA	NA
F <sub>5</sub>	December 2020	F-S	NA	NA	2020-12-20	NA	NA
G <sub>11</sub>	April 2021	P-I	Google Earth	NA	2021-04-28	NA	NA
G <sub>12</sub>	March 2022	P-I	Google Earth	NA	2022-03-23	NA	NA
G <sub>13</sub>	May 2023	P-I	Google Earth	NA	2023-05-30	NA	NA

#### 4 Multitemporal landslide inventory map

175 The multitemporal inventory includes 3,700 landslides (Fig. 3) corresponding to an average density of about 46.8 landslides per square kilometer. The total landslide area is equal to 17.15 km<sup>2</sup>, which represents 21.71 % of the study area. In this section the inventory will be analytically described. Section 4.1 to 4.3 describe landslides classified according to their relative age, type classification, and estimated depth (Cruden and Varnes, 1996). Landslide age, activity, and depth were determined based on the type of movement, the morphological characteristics and appearance of the landslides on the aerial photographs, the local lithological and structural setting, and the date of the aerial photographs.

180 The smallest landslide area is equal to 14.14 m<sup>2</sup> and the maximum is equal to 1,459,949.70 m<sup>2</sup>, the smallest landslide was identified in the Google Earth image taken on April 2021 (G<sub>11</sub> in tables 1 and 2); the largest landslide was identified using aerial the photographs taken in 1941 (A<sub>0</sub> in tables 1 and 2).



185 **Figure 3: Collazzone study area: multi temporal landslide inventory map. The landslides are represented by relative age. The black rectangle (A) shows the location of the enlargement of the map showing the abundance of the landslides over time (B).**

**Table 2. Descriptive statistics of landslides by relative age. ELA: estimated landslide age. The letters from A to E indicate the layer prepared by the photointerpretation of the stereo-aerial photographs. The letter F indicates the layers prepared through field surveys. The letter G indicates the layer prepared using satellite imagery.**

LAYER	ELA	Number	Total area (m <sup>2</sup> )	Minimum area (m <sup>2</sup> )	Maximum area (m <sup>2</sup> )
A <sub>0</sub>	very old, relict	27	5,722,962.53	63,092.20	1,459,949.69
A <sub>1</sub>	older than 1941	269	6,550,354.74	830.90	173,517.98
A <sub>2</sub>	1941	706	4,099,520.58	214.98	75,256.31
B <sub>1</sub>	1941–1954	63	423,474.99	863.68	22,780.15
B <sub>2</sub>	1954	97	706,685.96	771.98	49,705.96
C <sub>1</sub>	1954-1977	408	1,491,641.36	225.12	38,712.36
C <sub>2</sub>	1977	251	695,752.32	156.10	18,407.69
D <sub>1</sub>	1977-1985	105	618,621.79	782.33	33,350.85
D <sub>2</sub>	1985	135	450,435.24	102.67	27,018.30



E <sub>1</sub>	1985-1997	63	267,902.39	320.61	35,732.86
E <sub>2</sub>	1997	411	774,279.03	77.97	44,335.02
F <sub>1</sub>	1999-2000	17	70,319.46	136.84	26,055.11
F <sub>2</sub>	May 2004	70	266,827.73	97.31	31,909.89
F <sub>3</sub>	December 2004	168	385,104.39	51.49	47,884.06
F <sub>4</sub>	December 2005	60	179,790.55	35.86	57,080.83
G <sub>1</sub>	Sept-Mar 2010	161	294,191,82	36.95	15,118.84
G <sub>2</sub>	Apr-May 2010	55	83,792,35	29.83	11,562.11
G <sub>3</sub>	April 2011	1	1,097.07	1,097.07	1,097.07
G <sub>4</sub>	May 2012	6	5,703.18	232.32	1,929.69
G <sub>5</sub>	April 2013	108	121,255.22	47.51	10,395.81
G <sub>6</sub>	April 2014	217	283,384.61	16.82	13,440.34
G <sub>7</sub>	March 2015	103	120,783.43	32.09	8,896.57
G <sub>8</sub>	July 2015	14	7,542.02	87.01	2,086.68
G <sub>9</sub>	April 2018	16	8,387.12	40.60	2,160.92
G <sub>10</sub>	October 2019	14	9,846.33	31.88	4,048.00
F <sub>5</sub>	December 2020	21	19,406.15	90.89	3,205.30
G <sub>11</sub>	April 2021	128	153,080.5	14.14	7,882.60
G <sub>12</sub>	March 2022	3	1,392.06	143.75	673.67
G <sub>13</sub>	May 2023	3	1,426.57	106.10	704.68

190 In the multitemporal landslides inventory map each landslide is identified, in each layer, by a unique number. The attribute table of each layer includes three fields: N (identifier of each landslide); code (legend code); legend (extended legend of the code). Appendix A illustrates the explanation of the code and legend.

In the following the classification criteria used to describe the landslides are illustrated: i) age, iv) type, and iii) estimated depth.

#### 195 4.1 Landslide by age

Based on their appearance in aerial photographs, landslides were classified according to their relative age, namely (i) very old relict landslides, (ii) very old landslides, (iii) landslides among two consecutive aerial photographs data, (iv) landslides active at the data of the aerial photograph, v) landslides recognized in the field and dated considering the rainfall occurred immediately before the field survey and vi) landslides recognized in Google Earth images dated in the proximity of the  
 200 image. (Fig. 4). The four relative age levels (i), (ii), (iii) and (iv) refer to the general morphologic appearance of landslides

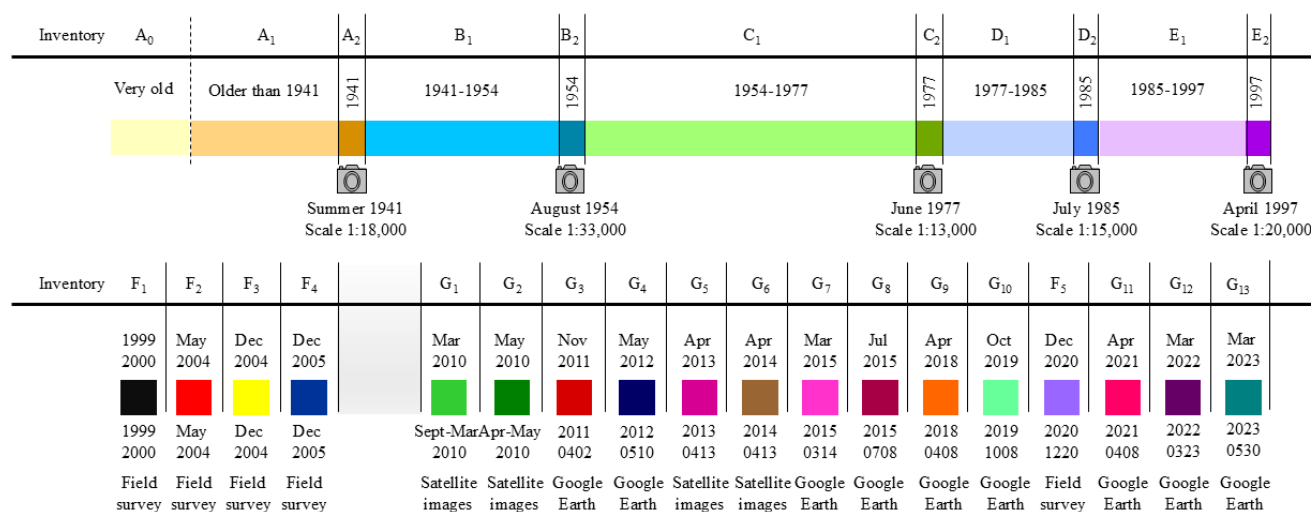


(Keaton and DeGraff, 1996) and assume that evidence of landslides becomes less obvious with increasing age, due, for example, to erosion processes, vegetation growth, occurrence of other landslides or human activity such as example ploughing, excavation, urbanization and restoration. Hence, older landslides are more difficult to detect than more recent ones as described by Ardizzone et al., 2023.

205 In each of the five sets of aerial photographs, landslides that appeared “fresh” (i.e. active) on the aerial photographs were separated from the other landslides. The date (i.e., year) of the aerial photographs used to identify the landslides was assigned to the “fresh” landslides, while the period between two successive sets of aerial photographs was attributed at the other slope failures (i.e., the “non-fresh” landslides). It is worth noting that the exact or approximate age of the landslides is undetermined, and it is inferred to be intermediate between the dates of the aerial photographs used to identify the landslides.

210 Event landslides were triggered by a known trigger (e.g., a rapid snowmelt event (Mauro Cardinali et al., 2000), a rainfall event (Ardizzone et al., 2007) and were identified and mapped using a single set of aerial photographs taken shortly after the event (see layer E<sub>2</sub> in Fig. 5 and table 1), or during a single field campaign. Event landslides pertaining to a single temporal layer of the multi-temporal inventory are of the same age, inferred from the date of the event, or the date of the aerial photographs or the field campaign. We started by identifying landslides on the 1954 aerial photographs (1:33,000) in

215 comparison with the 1941 aerial photographs. The photographs taken in 1954 are suitable for the identification of landslides, because the flight took place before the intensive post-war agricultural exploitation in Italy and prior to the widespread reforestation that has since increased forest cover in Italy, then we analyzed the other sets of aerial photographs to prepare separate landslide inventory maps (Fig. 4 and table 1).

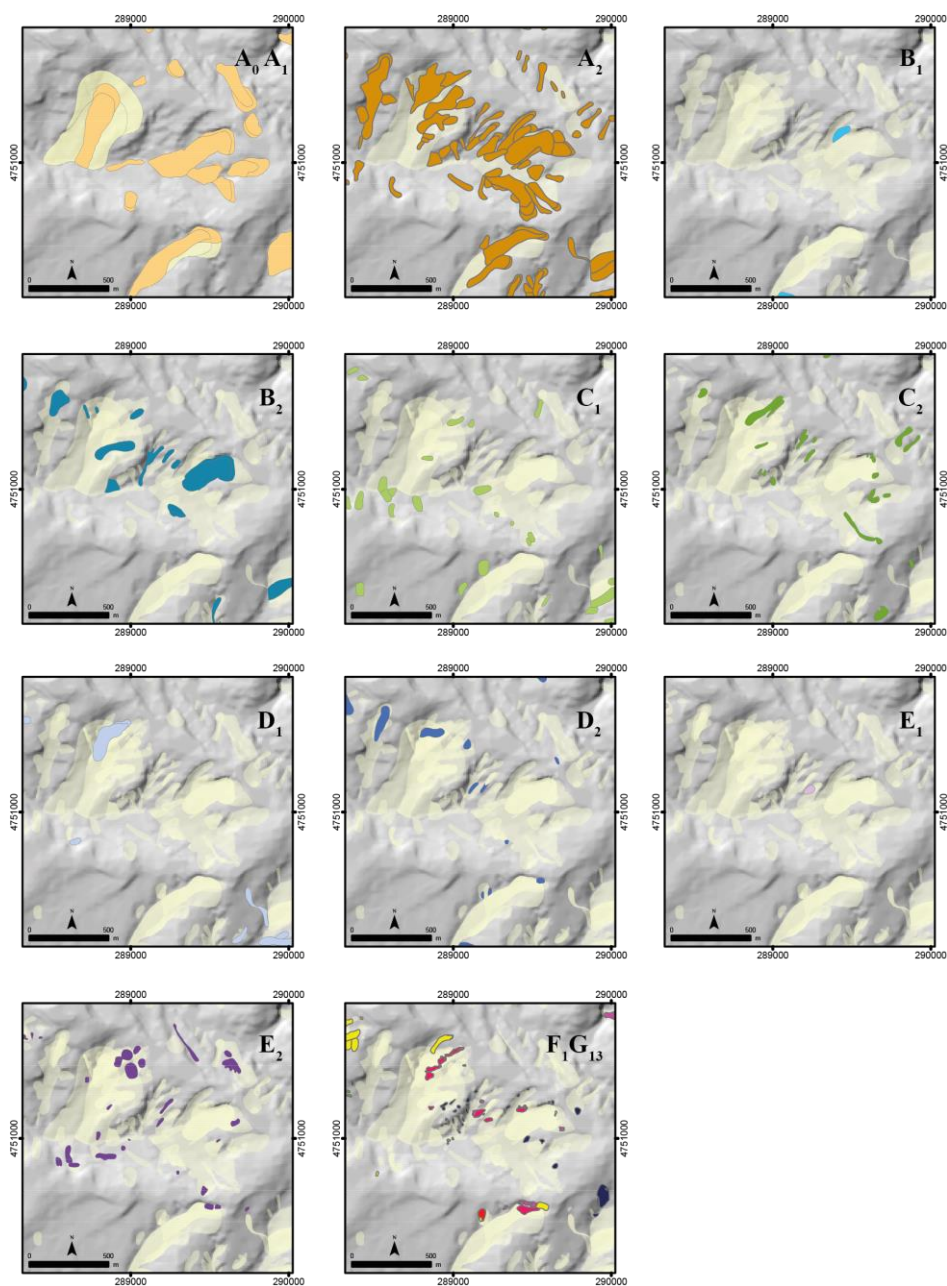


220 **Figure 4: Timeline showing the age attributed at the landslide layers. See table 1 for explanation of the layers.**



Figure 5 shows an enlargement of the M-LIM-C from very old ( $A_0$ ), old (preexisting the 1941) in the panel  $A_0A_1$  to the landslides observed during the field surveys and using satellite tools (i.e. stereo satellite images and Google Earth images) after the 1997 in the panel  $F_1G_{13}$ .

The figures 3 and 5 highlights that in the period of more of about 80 years (1941-2023) the temporal recurrence has high  
225 frequency and that landslides tend to occur where previous landslides occurred due to a legacy effect (Samia et al., 2017b).





230

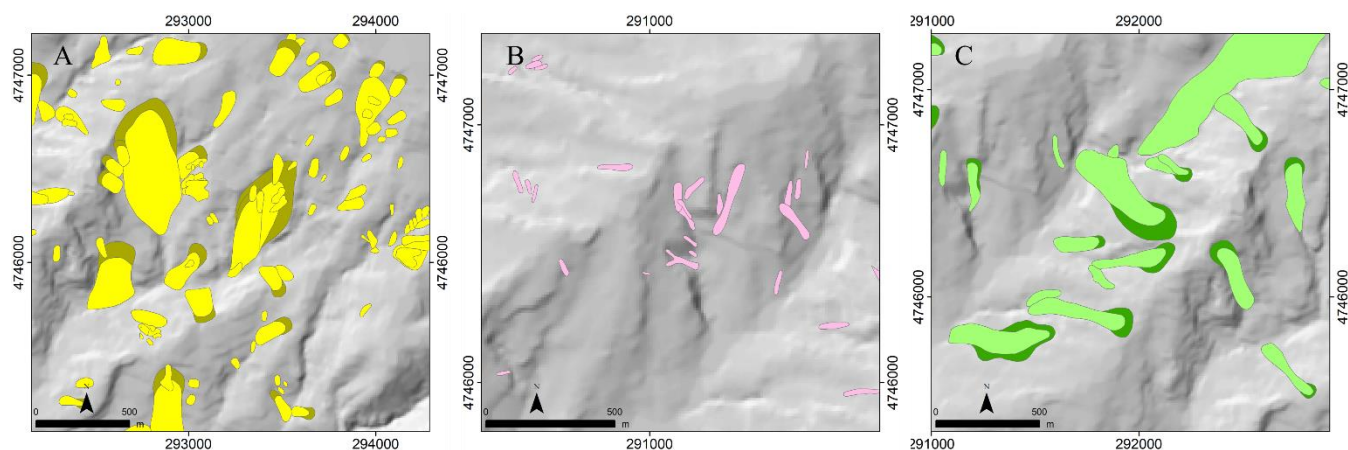
**Figure 5: Enlargement of a portion of study area. The letters indicate the layers of the multitemporal inventory map (table 1 and figure 4). The panels show: A<sub>0</sub>A<sub>1</sub>) very old and old landslides; A<sub>2</sub>) fresh landslides in 1941 photographs; B<sub>1</sub>) landslides occurred between 1941 and 1954; B<sub>2</sub>) fresh landslides in 1954 photographs; C<sub>1</sub>) landslides occurred between 1954 and 1977; C<sub>2</sub>) fresh landslides in 1977 photographs; D<sub>1</sub>) landslides occurred between 1977 and 1985; D<sub>2</sub>) fresh landslides in 1985 photographs; E<sub>1</sub>) landslides occurred between 1985 and 1997; E<sub>2</sub>) fresh landslides in 1997 photographs and F<sub>1</sub>G<sub>4</sub>) landslides occurred from 1997 through 2023.**

## 4.2 Landslide by type

235

Landslide type included in the legend of the M-LIM-C are: (i) slide-type landslides (which include deep-seated slides and shallow soil slides), (ii) earth flow, (iii) slide-earth flow.

According to the type of movement, the most represented landslides in the study area are slides with 2787 landslides (example in Fig. 6A), whereas earth flows and slide-earth flows (examples in Fig. 6B and Fig. 6C) are represented by 507 and 352 landslides respectively.



240

**Figure 6: Enlargement of a portion of study area. Landslide examples of landslide type. A) slide; B) earth flow; C) slide-earth flow.**

245

The slides present a well-defined scarp which can be semi-circular (rotational slides) or angular (translational slides). The slide deposit is convex, with a morphologically depressed head of the deposit characterized by a centripetal drainage and local counter-slopes and a toe characterized by a typical upward bulge. Earth flows are characterized by an overall elongated planar shape, with the median part narrower than the detachment and accumulation zones. Slide-earth flows (Fig. 6c, d) start as slides and then evolve into flows. Therefore, they show the characteristics of slides (most commonly rotational) in the escarpment area and in the head of the deposit, on the other hand, the transport zone and accumulation zone are more like earth flows.

## 4.3 Landslide by estimated depth

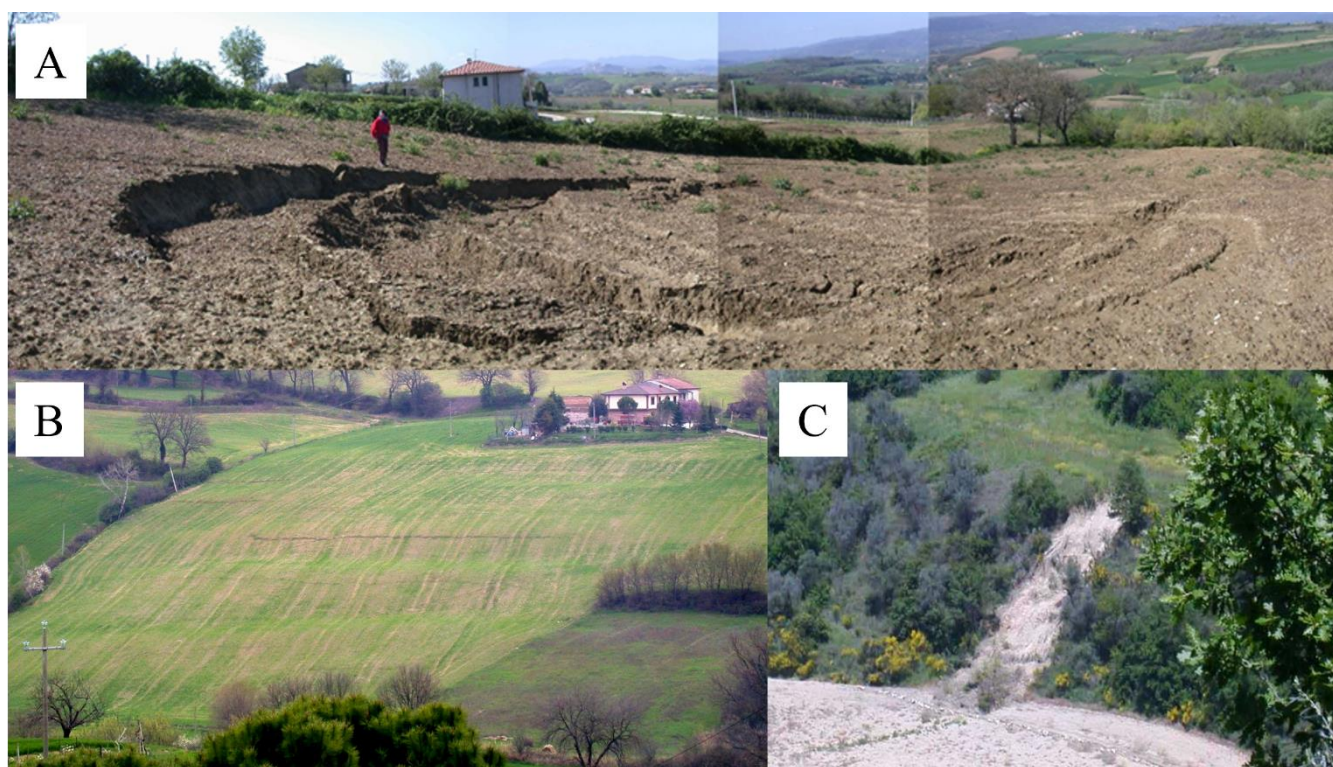
250

The estimated depth of a landslide is assigned based on the main morphological characteristics of the landslide, such as slope height, and the extent of curvatures along the slope (convexity and concavity). Based on these morphological characteristics, landslides were classified as deep-seated or shallow. For deep-seated slope failures, the landslide crown was mapped



separately from the deposit. The distinction was not made for the shallow landslides. Many of the deep-seated landslides can be classified as very old and older than 1941 landslides. They often involve considerable volumes of material and can alter the local morphology and geological structure. According to (Santangelo et al., 2015) the beddings condition the location and abundance of the deep-seated landslides, which are most abundant in cataclinal dip and under-dip slopes and does not condition significantly the distribution and abundance of the shallow landslides.

Figure 7 shows a deep-seated slide (A) and two shallow landslides (B and C).



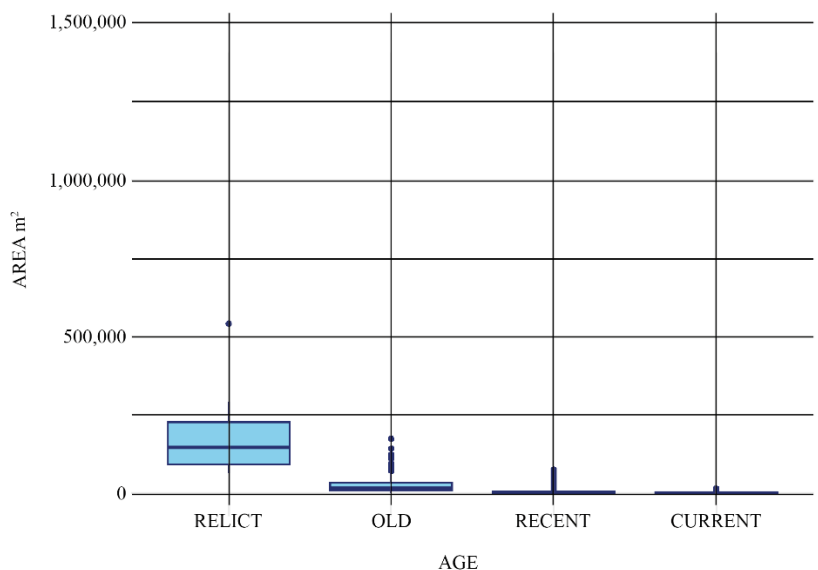
260 **Figure 7: Examples of landslide depth. A) deep-seated slide; B) soil slide; C) earth flow. The photographs were taken by the CNR-IRPI.**

#### 4.4 Descriptive statistics

Descriptive statistics in number and size (total, maximum and minimum area) of the landslides are shown in table 2 and in the box plots in Fig. 8a, b. Figure 8 shows the distribution of landslide areas for the landslides based on the age grouped on four classes of age: i) very old (relict) landslides; (ii) old landslides (landslides occurred before 1941); iii) recent landslides (landslides occurred between 1941 and December 2005) and iv) current landslides (occurred after December 2005). Figure 9 shows landslide count (represented by a color gradient and labels) and cumulated area (proportional to circle sizes), grouped by relative age class and landslide type.



270 The plot in Fig. 8 shows the size distribution of the four groups of landslides. The clear separation of the age groups according to their median values indicates that relict and old landslides have a median value higher than the median of recent and current landslides. That could be an indication that relict landslides were triggered in a different tectonic and climatic setting while recent and current landslides were triggered in a similar climatic setting. As far as concern the old landslides, probably they have triggered in a climate environment different from the others.



275 **Figure 8: Plots summarizing landslide statistics. Landslide area grouped by relative age class (relict; old; recent and current); (b)**

Figure 9 shows landslide count (represented by a color gradient and labels) and cumulated area (proportional to circle sizes), grouped by relative age class and landslide type. Visual inspection of the plot reveals that relict and very old landslides are mainly represented by small landslides represented by flows which tend to be small and easily obliterated by erosion and subsequent failures. Further evidence is that a large portion of the total landslide area is occupied by few relict landslides, whereas the smallest landslides correspond to the current period, according to the results by Ardizzone et al. (2023). They suggested that a size threshold effect of previous landslides on subsequent landslides.

280

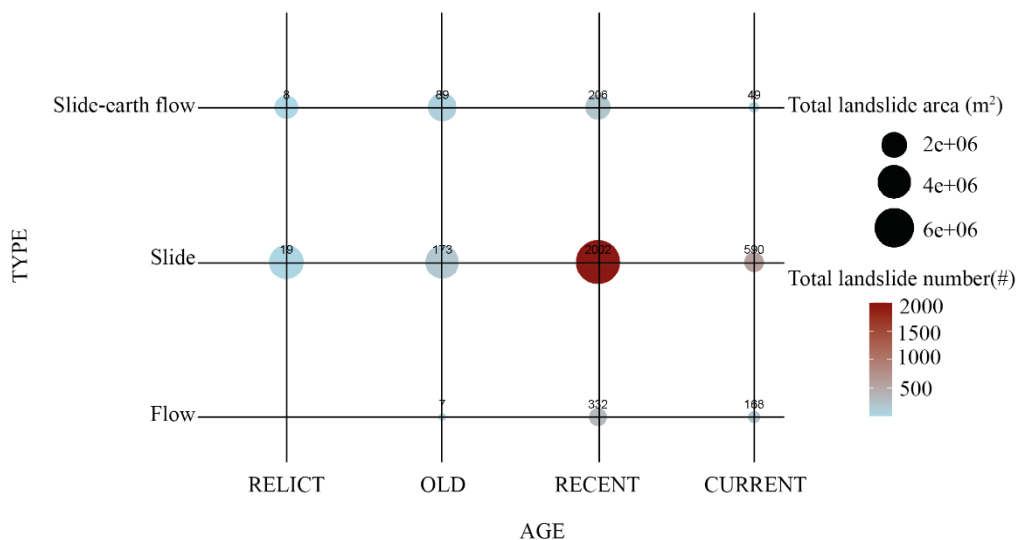


**Figure 9: Scatterplot showing cumulative sizes and counts of landslides grouped by relative age in the abscissa and type in the ordinate. Landslide number is represented by a color gradient and labels; total area is proportional to circle sizes.**

## 285 5 Quality control

The quality of a landslide inventory depends on its accuracy and the type and certainty of information shown on the map. Defining the accuracy of a landslide inventory is not straightforward, and there are no standards (Galli et al., 2008). Accuracy depends on the completeness of the map and the geographic and thematic correctness of the information displayed on the map. Galli et al. (2008) compared the multi-temporal landslide inventory map of Collazzone area, including landslides  
 290 until 2005, with two pre-existing landslide inventory maps for the same study area: a reconnaissance landslide inventory map and a geomorphological landslide inventory map (namely A1 and A2) prepared by photo interpretation of one and three sets of stereo aerial photographs respectively and very few field checks. The first test consisted of evaluating the degree of cartographic matching between the maps, comparing the inventories in pairs in a GIS. The overall error index (E) was calculated according to Ardizzone et al., 2002, using the equation (eq. 1):

295

$$E = \frac{(A1 \cup A2) - (A1 \cap A2)}{A1 \cup A2}, \text{ con } E \ 0 \leq E \leq 1 \quad (1)$$

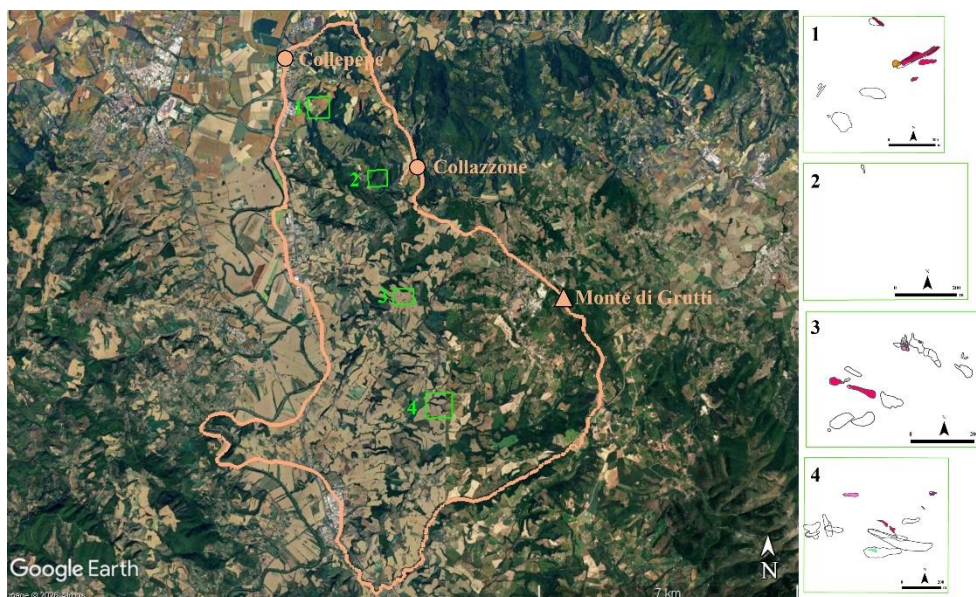
where A1 and A2 are the total landslide areas in the first and in the second inventory, respectively, and  $\cup$  and  $\cap$  are the geographical union and intersection of the two inventories, obtained in a GIS.

300 Mapping error ranges from 0.66 to 0.81, the overall mapping error is smallest (0.66) when the most accurate (multi-temporal landslide inventory) and the second most accurate (geomorphological inventory) inventories are compared. The error



includes: (i) uncertainties associated with the identification of the landslides, (ii) drafting and positional errors introduced when transferring the landslide information from the aerial photographs to the base map, (iii) digitization errors and other mistakes introduced in the construction of the digital cartographic database (Carrara et al., 1992). Moreover, the authors  
305 evaluated the drafting and digitization errors from the mismatch due to different geomorphological interpretations, the figures correspond to a cartographic error of approximately 2.5–5 %. The remaining mismatch (~62–75 %) was attributed to different geomorphological interpretations. The authors determined the frequency-area statistics of landslides and probability density function (pdf) obtained for the three landslide inventory maps differ significantly. The area of the most abundant landslides of the multi-temporal inventory is 815 m<sup>2</sup> that is less than the other two inventories, and the power-law exponent  
310 is also less than the other two. These figures indicate that the multi-temporal landslide inventory map contains a very large number of small size landslides.

To validate the landslides defined “current landslides” occurred after the 2005 an external geomorphologist investigated four geographical sectors, shown in figure 10, using Google Earth. Landslides from 2013, 2015, 2018, 2019, and 2021 were identified in sectors 1, 3, and 4. In sector 1 the geomorphologist didn’t recognize any landslide.



315

**Figure 10: Collazzone study area: localization of the four geographical sectors. Maps data: © Google Earth 2026; images: © 2026 Airbus. An independent geomorphologist investigated the images of different times in the four sectors. In the four sectors black lines show the landslides included in the multi-temporal landslide inventory map. Colored polygons represent the landslides mapped by the external geomorphologist.**

320 To analyze quantitatively the differences between the two inventories the overall error index (E) was calculated between landslides belonging to the same date. The results are shown in table 3. The overall error index varies between 0.06 and 0.77.



325 **Table 3. Overall error Index (E) calculated in four sectors of the study area (fig. 10). The values were calculated between the landslides of the multitemporal landslide inventory and the landslides identified by the external geomorphologist who had investigated Google Earth Images along time. ELA: estimated landslide age.**

LAYER	ELA	SECTOR 1	SECTOR 2	SECTOR 3	SECTOR 4
		E	E	E	E
G <sub>11</sub>	April 2021	0.38	NA	0.21	0.24
G <sub>10</sub>	October 2019	NA	NA	NA	0.26
G <sub>9</sub>	April 2018	0.16	NA	NA	NA
G <sub>8</sub>	July 2015	0.33	NA	NA	NA
G <sub>7</sub>	March 2015	NA	NA	0.68	0.77
G <sub>5</sub>	April 2013	NA	NA	NA	0.06

## 6 Conclusion

The multitemporal landslide inventory map presented in this paper is the result of mapping work that began around the year 2000. Even today, landslides in the Collazzone area are identified following intense or prolonged meteorological events. The  
330 landslide inventory was produced in the framework of free scientific research initially to deepen knowledge from a geological and geomorphological point of view of a hilly area intended mainly for agricultural use to reconstruct the evolution of the landscape. During the preparation of the inventory map, it became clear that this information could be used to develop models for zoning landslide hazard and risk.

Galli et al., 2008, established that the multitemporal inventory in Collazzone represents a significant improvement upon the  
335 geomorphological and reconnaissance inventories. In this work the authors proposed a framework for a quantitative comparison of landslide inventory maps through several tests. However, due to the time and the resources required to complete a multi-temporal inventory, such type of detailed mapping cannot be effectively prepared for a large region, extending for thousands of square kilometers, even though any landslide hazard evaluation requires considering the temporal behavior of the landslides. For the current landslides a comparison between the landslides of the multitemporal landslide  
340 inventory and the landslides identified by the external geomorphologist in four sectors was carried out. Findings revealed an overall index error ranging from 0.06 to 0.77.

The availability of this inventory has enabled many researchers from international institutions to conduct research curiosity driven as proved by numerus published papers (Samia et al., 2020; Lombardo et al., 2020b; Samia et al., 2018, 2017a; Rossi et al., 2010; Samia et al., 2017b; Guzzetti et al., 2009b; Galli et al., 2008; Guzzetti et al., 2006c).

345



## 6 Data availability

The dataset is available in ZENODO repository DOI: <https://doi.org/10.5281/zenodo.18980281> (Ardizzone, 2026).

## Author contribution

We declare that all the authors' contributions in preparing both the dataset and the manuscript are equivalent to that of a first  
350 author. This is why all the authors appear in alphabetical order.

## Financial support

This work did not receive external funds

## Competing interests

The authors declare that they have no conflict of interest.

## 355 Acknowledgement

Mirco Galli, Fausto Guzzetti, Paola Reichenbach, Michele Santangelo, Francesco Bucci and the geomorphological group of  
CNR-IRPI (Perugia, Italy).

## References

- 360 Amatya, P., Emberson, R., and Kirschbaum, D.: Multitemporal landslide inventory and susceptibility map for the Arun River  
Basin, Nepal, *Geoscience Data Journal*, *gdj3.240*, <https://doi.org/10.1002/gdj3.240>, 2024.
- Ardizzone Francesca: Multitemporal Landslide Inventory Map of Collazzone study area (Italy) [Data set].  
Zenodo. <https://doi.org/10.5281/zenodo.18980281>, 2026.
- Ardizzone, F., Cardinali, M., Carrara, A., Guzzetti, F., and Reichenbach, P.: Impact of mapping errors on the reliability of  
landslide hazard maps, *Nat. Hazards Earth Syst. Sci.*, *2*, 3–14, <https://doi.org/10.5194/nhess-2-3-2002>, 2002.
- 365 Ardizzone, F., Cardinali, M., Galli, M., Guzzetti, F., and Reichenbach, P.: Identification and mapping of recent rainfall-  
induced landslides using elevation data collected by airborne Lidar, *Nat. Hazards Earth Syst. Sci.*, *7*, 637–650,  
<https://doi.org/10.5194/nhess-7-637-2007>, 2007.
- Ardizzone, F., Fiorucci, F., Santangelo, M., Cardinali, M., Mondini, A. C., Rossi, M., Reichenbach, P., and Guzzetti, F.:  
370 Very-High Resolution Stereoscopic Satellite Images for Landslide Mapping, in: *Landslide Science and Practice*, edited by:  
Margottini, C., Canuti, P., and Sassa, K., Springer Berlin Heidelberg, Berlin, Heidelberg, 95–101,  
[https://doi.org/10.1007/978-3-642-31325-7\\_12](https://doi.org/10.1007/978-3-642-31325-7_12), 2013.



- Ardizzone, F., Bucci, F., Cardinali, M., Fiorucci, F., Pisano, L., Santangelo, M., and Zumpano, V.: Geomorphological landslide inventory map of the Daunia Apennines, southern Italy, *Earth Syst. Sci. Data*, 15, 753–767, <https://doi.org/10.5194/essd-15-753-2023>, 2023.
- 375 Bhuyan, K., Tanyaş, H., Nava, L., Puliero, S., Meena, S. R., Floris, M., Van Westen, C., and Catani, F.: Generating multi-temporal landslide inventories through a general deep transfer learning strategy using HR EO data, *Sci Rep*, 13, 162, <https://doi.org/10.1038/s41598-022-27352-y>, 2023a.
- Bhuyan, K., Meena, S. R., Nava, L., Van Westen, C., Floris, M., and Catani, F.: Mapping landslides through a temporal lens: an insight toward multi-temporal landslide mapping using the u-net deep learning model, *GIScience & Remote Sensing*, 60, 2182057, <https://doi.org/10.1080/15481603.2023.2182057>, 2023b.
- 380 Cardinali, M., Reichenbach, P., Guzzetti, F., Ardizzone, F., Antonini, G., Galli, M., Cacciano, M., Castellani, M., and Salvati, P.: A geomorphological approach to the estimation of landslide hazards and risks in Umbria, Central Italy, *Nat. Hazards Earth Syst. Sci.*, 2, 57–72, <https://doi.org/10.5194/nhess-2-57-2002>, 2002.
- Cardinali, M., Galli, M., Guzzetti, F., Ardizzone, F., Reichenbach, P., and Bartoccini, P.: Rainfall induced landslides in December 2004 in south-western Umbria, central Italy: types, extent, damage and risk assessment, *Nat. Hazards Earth Syst. Sci.*, 6, 237–260, <https://doi.org/10.5194/nhess-6-237-2006>, 2006.
- 385 Cardinali, M., Galli, M., Ardizzone, F., Guzzetti, F., and Reichenbach, P.: Comparing landslide rates in the northern and central Apennines, Italy, in: *Geophysical Research Abstracts, European Geosciences Union 2007*, 2007.
- Carrara A., Cardinali M., and Fausto Guzzetti: Uncertainty in assessing landslide hazard and risk, *ITC Journal*, 172–183, 1992.
- 390 Cruden, D. and Varnes, D.: Landslide types and processes. In Turner, AK and Schuster, RL (eds.), *Landslides-Investigation and Mitigation*. Washington DC, National Academy Press, Transportation Research Board Special Report 247, pp. 36-75., 1996.
- Del Ventisette, C., Righini, G., Moretti, S., and Casagli, N.: Multitemporal landslides inventory map updating using spaceborne SAR analysis, *International Journal of Applied Earth Observation and Geoinformation*, 30, 238–246, <https://doi.org/10.1016/j.jag.2014.02.008>, 2014.
- 395 Fernández, T., Pérez-García, J. L., Gómez-López, J. M., Cardenal, J., Moya, F., and Delgado, J.: Multitemporal Landslide Inventory and Activity Analysis by Means of Aerial Photogrammetry and LiDAR Techniques in an Area of Southern Spain, *Remote Sensing*, 13, 2110, <https://doi.org/10.3390/rs13112110>, 2021.
- 400 Fiorucci, F., Cardinali, M., Carlà, R., Rossi, M., Mondini, A. C., Santurri, L., Ardizzone, F., and Guzzetti, F.: Seasonal landslide mapping and estimation of landslide mobilization rates using aerial and satellite images, *Geomorphology*, 129, 59–70, <https://doi.org/10.1016/j.geomorph.2011.01.013>, 2011.
- Galli, M., Ardizzone, F., Cardinali, M., Guzzetti, F., and Reichenbach, P.: Comparing landslide inventory maps, *Geomorphology*, 94, 268–289, <https://doi.org/10.1016/j.geomorph.2006.09.023>, 2008.
- 405 Guzzetti, F., Cardinali, M., Reichenbach, P., and Carrara, A.: Comparing Landslide Maps: A Case Study in the Upper Tiber River Basin, Central Italy, *Environmental Management*, 25, 247–263, <https://doi.org/10.1007/s002679910020>, 2000.
- Guzzetti, F., Reichenbach, P., Cardinali, M., Galli, M., and Ardizzone, F.: Probabilistic landslide hazard assessment at the basin scale, *Geomorphology*, 72, 272–299, <https://doi.org/10.1016/j.geomorph.2005.06.002>, 2005.



- 410 Guzzetti, F., Reichenbach, P., Ardizzone, F., Cardinali, M., and Galli, M.: Estimating the quality of landslide susceptibility models, *Geomorphology*, 81, 166–184, <https://doi.org/10.1016/j.geomorph.2006.04.007>, 2006a.
- Guzzetti, F., Galli, M., Reichenbach, P., Ardizzone, F., and Cardinali, M.: Landslide hazard assessment in the Collazzone area, Umbria, Central Italy, *Natural hazards and earth system sciences*, 6, 115–131, 2006b.
- Guzzetti, F., Galli, M., Reichenbach, P., Ardizzone, F., and Cardinali, M.: Landslide hazard assessment in the Collazzone area, Umbria, Central Italy, *Nat. Hazards Earth Syst. Sci.*, 6, 115–131, <https://doi.org/10.5194/nhess-6-115-2006>, 2006c.
- 415 Guzzetti, F., Reichenbach, P., Ardizzone, F., Cardinali, M., and Galli, M.: Landslide hazard assessment, vulnerability estimation and risk evaluation. An example from the Collazzone Area (Central Umbria, Italy), *eogr Fis Dinam Quat*, 32, 183–192, 2009a.
- Guzzetti, F., Ardizzone, F., Cardinali, M., Rossi, M., and Valigi, D.: Landslide volumes and landslide mobilization rates in Umbria, central Italy, *Earth and Planetary Science Letters*, 279, 222–229, <https://doi.org/10.1016/j.epsl.2009.01.005>, 2009b.
- 420 Guzzetti, F., Mondini, A. C., Cardinali, M., Fiorucci, F., Santangelo, M., and Chang, K.-T.: Landslide inventory maps: New tools for an old problem, *Earth-Science Reviews*, 112, 42–66, <https://doi.org/10.1016/j.earscirev.2012.02.001>, 2012.
- Li, P., Wang, Y., Liu, G., Fang, Z., and Ullah, K.: Unsupervised Landslide Detection From Multitemporal High-Resolution Images Based on Progressive Label Upgradation and Cross-Temporal Style Adaption, *IEEE Trans. Geosci. Remote Sensing*, 62, 1–15, <https://doi.org/10.1109/TGRS.2024.3425863>, 2024.
- 425 Lombardo, L., Opitz, T., Ardizzone, F., Guzzetti, F., and Huser, R.: Space-time landslide predictive modelling, *Earth-Science Reviews*, 209, 103318, <https://doi.org/10.1016/j.earscirev.2020.103318>, 2020a.
- Lombardo, L., Opitz, T., Ardizzone, F., Guzzetti, F., and Huser, R.: Space-time landslide predictive modelling, *Earth-Science Reviews*, 209, 103318, <https://doi.org/10.1016/j.earscirev.2020.103318>, 2020b.
- 430 Mauro Cardinali, Francesca Ardizzone, Mirco Galli, Fausto Guzzetti, and Paola Reichenbach: Landslides triggered by rapid snow melting: the December 1996-January 1997 event in Central Italy, in: *Proceedings 1st Plinius conference on Mediterranean storms, 1st Plinius conference on Mediterranean storms*, 439–448, 2000.
- Mergili, M., Marchesini, I., Alvioli, M., Metz, M., Schneider-Muntau, B., Rossi, M., and Guzzetti, F.: A strategy for GIS-based 3-D slope stability modelling over large areas, *Geosci. Model Dev.*, 7, 2969–2982, <https://doi.org/10.5194/gmd-7-2969-2014>, 2014.
- 435 Pašek, J.: Landslides inventory, *Bulletin of the International Association of Engineering Geology*, 12, 73–74, <https://doi.org/10.1007/BF02635432>, 1975.
- Rossi, M., Guzzetti, F., Reichenbach, P., Mondini, A. C., and Peruccacci, S.: Optimal landslide susceptibility zonation based on multiple forecasts, *Geomorphology*, 114, 129–142, <https://doi.org/10.1016/j.geomorph.2009.06.020>, 2010.
- 440 Samia, J., Temme, A., Bregt, A., Wallinga, J., Guzzetti, F., Ardizzone, F., and Rossi, M.: Characterization and quantification of path dependency in landslide susceptibility, *Geomorphology*, 292, 16–24, <https://doi.org/10.1016/j.geomorph.2017.04.039>, 2017a.
- Samia, J., Temme, A., Bregt, A., Wallinga, J., Guzzetti, F., Ardizzone, F., and Rossi, M.: Do landslides follow landslides? Insights in path dependency from a multi-temporal landslide inventory, *Landslides*, 14, 547–558, <https://doi.org/10.1007/s10346-016-0739-x>, 2017b.



- 445 Samia, J., Temme, A., Bregt, A. K., Wallinga, J., Stuiver, J., Guzzetti, F., Ardizzone, F., and Rossi, M.: Implementing landslide path dependency in landslide susceptibility modelling, *Landslides*, 15, 2129–2144, <https://doi.org/10.1007/s10346-018-1024-y>, 2018.
- Samia, J., Temme, A., Bregt, A., Wallinga, J., Guzzetti, F., and Ardizzone, F.: Dynamic path-dependent landslide susceptibility modelling, *Nat. Hazards Earth Syst. Sci.*, 20, 271–285, <https://doi.org/10.5194/nhess-20-271-2020>, 2020.
- 450 Santangelo, M., Marchesini, I., Cardinali, M., Fiorucci, F., Rossi, M., Bucci, F., and Guzzetti, F.: A method for the assessment of the influence of bedding on landslide abundance and types, *Landslides*, 12, 295–309, <https://doi.org/10.1007/s10346-014-0485-x>, 2015.
- Santangelo, M., Althuwaynee, O., Alvioli, M., Ardizzone, F., Bianchi, C., Bornaetxea, T., Brunetti, M. T., Bucci, F., Cardinali, M., Donnini, M., Esposito, G., Gariano, S. L., Grita, S., Marchesini, I., Melillo, M., Peruccacci, S., Salvati, P., Yazdani, M., and Fiorucci, F.: Inventory of landslides triggered by an extreme rainfall event in Marche-Umbria, Italy, on 15 September 2022, *Sci Data*, 10, 427, <https://doi.org/10.1038/s41597-023-02336-3>, 2023.
- Zumpano, V., Ardizzone, F., Bucci, F., Cardinali, M., Fiorucci, F., Parise, M., Pisano, L., Reichenbach, P., Santaloia, F., Santangelo, M., Wasowski, J., and Lollino, P.: The relation of spatio-temporal distribution of landslides to urban development (a case study from the Apulia region, Southern Italy), *Journal of Maps*, 17, 133–140, <https://doi.org/10.1080/17445647.2020.1746417>, 2021.
- 460